Open Access

Schottky-Barrier Photodiode Internal Quantum Efficiency Dependence on Nickel Silicide Film Thickness

Joshua Duran
Andrew Sarangan
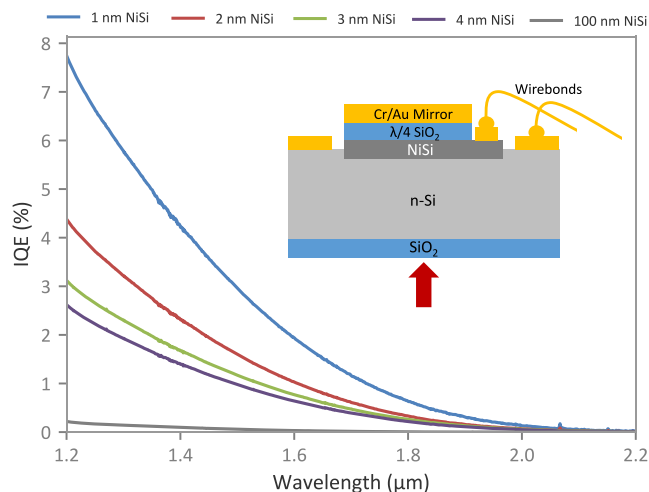
Schottky-Barrier Photodiode Internal Quantum Efficiency Dependence on Nickel Silicide Film Thickness

Joshua Duran [1,2] **and Andrew Sarangan** [2]

[1]Air Force Research Laboratory, Sensors Directorate, Ohio, OH 45433 USA
[2]Department of Electro-Optics and Photonics, University of Dayton, Dayton, OH 45469 USA

Abstract: In this paper we show that the internal quantum efficiency of NiSi Schottky-barrier photodetectors can be significantly improved as the silicide film thickness is reduced close to its percolation threshold. We fabricated photodetectors in two optical configurations (front-side and back-side illuminated) at four different film thicknesses between 1–4 nm as well as a thick (100 nm) reference device. We simultaneously fit the reflection and transmission data for each silicide film on silicon as well as for front and backside illuminations to extract the refractive index dispersion of each film. Using this technique, we can accurately determine the absorption of each constituent layer and extract the wavelength-dependent internal quantum efficiency from the external quantum efficiency. We show that the internal quantum efficiency is highly dependent on the silicide film thickness while the dark current is not. The internal quantum efficiency of our thinnest detector is the highest reported of any silicide Schottky-barrier photodetector of comparable barrier height to date with a $57\times$ improvement over the thick (reference) device. Using an approximation to Vickers' model, we were able to fit the IQE spectra to extract the hot carrier mean-free path of electrons in NiSi.

Index Terms: Infrared photodetector, Schottky-barrier, photodiode, NiSi, quantum efficiency, silicide, thickness dependence, hot carrier attenuation length, hot carrier mean-free path, absorption.

1. Background and Motivation

Silicide-based Schottky-barrier detectors (SBDs) are an enticing approach to infrared detection beyond the bandgap of silicon. The most intriguing feature of these detectors is their natural integration into the silicon complementary metal-oxide semiconductor (CMOS) fabrication process. CMOS compatibility enables monolithic integration of the SBD with logic signal conditioning circuitry, enabling the development of novel optoelectronic chips for applications such as telecommunications and infrared imaging. Unlike narrow bandgap semiconductor-based detectors such as Ge or InGaAs, there is no lattice matching constraint for the integration of silicide SBDs directly onto crystalline silicon. The silicide formation is done at relatively low temperatures, making it possible to integrate these devices into back end of line (BEOL) process steps. This attribute can simplify and dramatically reduce the fabrication cost of detector arrays and opto-electronic integrated circuits. Early development of SBDs was focused on Pd_2Si [1], [2], PtSi [3]–[7] and IrSi [8]–[11] on p-type
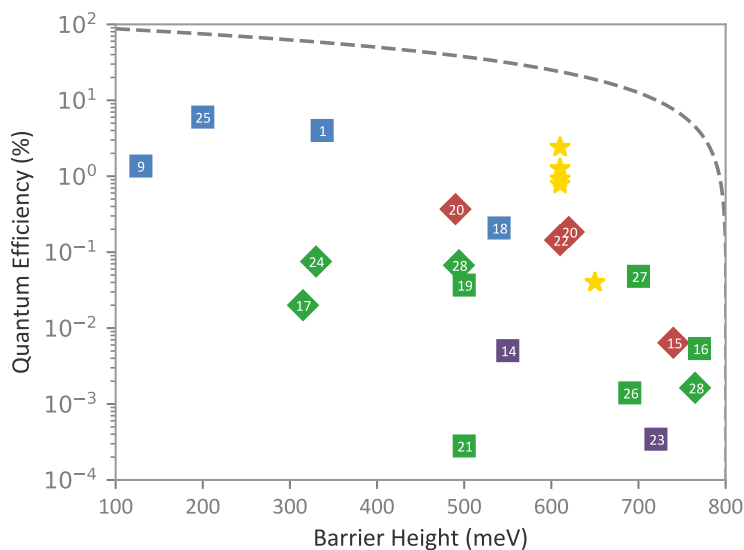
Fig. 1. Reported external (square) and internal (diamond) quantum efficiency for various metal/metal-silicide Schottky-barrier photodetectors at 1.55 μm [1], [9], [14]–[28]. Blue marker-fill indicates standard front-side or back-side illuminated detectors, green indicates plasmonic resonant detectors, red indicates waveguide integrated detectors and purple indicates resonant-cavity-enhanced detectors. Yellow stars designate internal quantum efficiency results from this work. The dashed line represents the theoretical maximum quantum efficiency based on the barrier height, assuming a sharp emission threshold [29].

Si for passive imaging applications in the 1–3 μm, 3–5 μm and 8–12 μm atmospheric transmission windows respectively. However, the relatively small Schottky-barrier height (SBH) of these detectors (0.1–0.35 eV) requires cryogenic cooling to manage the detector dark current driven by thermionic emission [12], [13]. This cooling requirement has limited the utility of these detectors for low-cost consumer-based applications. More recent work has explored a variety of metals and silicides with larger barrier heights for room temperature operation on both n and p type substrates. Larger SBH translates to lower detector dark current (and therefore higher operating temperature), but also reduces detector quantum efficiency (QE) at a given wavelength. Poor QE relative to semiconductor bandgap-based detectors has been the primary challenge in the development of SBDs, and has inhibited its widespread use.

Fig. 1 shows a collection of reported QE values at 1.55 μm for a variety of SBDs; purposely omitted from this collection are detectors featuring internal gain, which obfuscates the device QE. When available, the internal quantum efficiency (IQE), which is analogous to collection efficiency here, is plotted. Included in this collection are novel structures designed to improve QE by increasing absorption such as plasmonic resonators, waveguide integrated devices and photonic resonant cavities. Despite these novel device designs, reported QE and IQE values are often orders of magnitude below the theoretical maximum (hence the need for a logarithmic y-axis).

Fig. 1 shows the general trend of increasing QE with decreasing SBH, as expected. To interrogate the effect of silicide thickness on QE, we calculate the ratio of the reported QE to the theoretical maximum (to minimize the barrier height influence) and plot that result vs the reported silicide thickness (Fig. 2). From this plot it becomes clear that silicide thickness is the most critical design parameter for maximizing the QE of SBDs. The highest performing SBDs to date feature very thin silicide layers, leading to relatively simple backside-illuminated architectures with incomplete absorption outperforming novel resonant and waveguide architectures. Improved QE in thin silicide layers was first reported by Kimata *et al.* [6] in PtSi where they found a thin 9 nm silicide (the thinnest device tested in that work) exhibited the highest QE. Higher performance was subsequently reported for PtSi layers as thin as 2 nm [25]. This improvement has been attributed to multiple interface reflections of hot carriers when the silicide thickness is reduced below the hot carrier
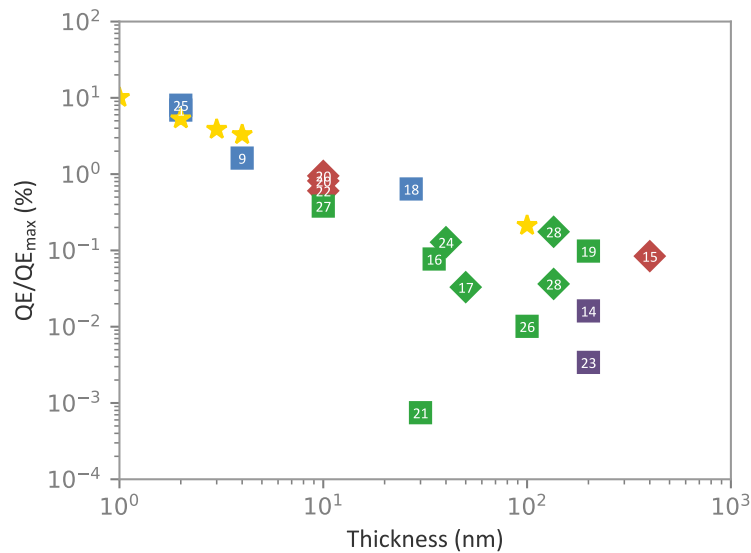
Fig. 2. Same collection of reported quantum efficiency values from Fig. 1, but plotted as a function of the reported metal/metal-silicide thickness. In an effort to minimize the barrier height influence, the quantum efficiency is divided by the theoretical maximum (based on the barrier height). The marker color and shape are the same indicators as in Fig. 1.
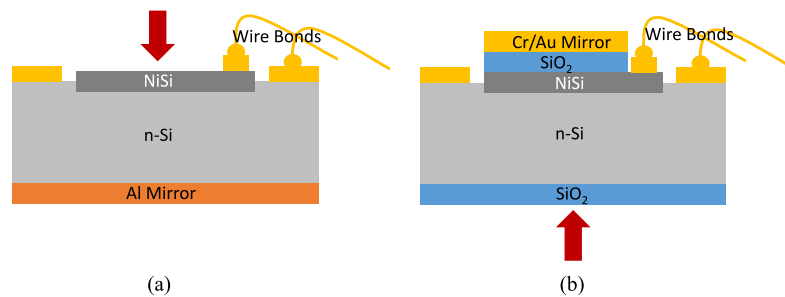

Fig. 3. Schematic of (a) FSI and (b) BSI photodetectors. Detectors are square shaped ranging in width between 500 and 1000 μm. 100 μm square top contact bond pads and large area ground metal surrounding the detector are wire bonded to a ceramic chip carrier for device testing.

mean-free path [6], [29]. Despite the age of this fundamental knowledge, very few reports of SBDs with thickness below 10 nm exist, and to our knowledge thickness dependence on QE has been systematically studied and reported for PtSi alone (3–5 μm wavelength). The purpose of this paper is to investigate the QE thickness dependence of NiSi on n-type Si. This material system is important because its approximately 600 meV barrier height covers the short-wave infrared and telecom wavelengths while maintaining a reasonably low dark current density at room temperatures. Because IQE monotonically increases towards the theoretical limit with decreasing silicide thickness [29], our goal is to fabricate and characterize devices that approach the minimum achievable film thickness (which is determined by the percolation threshold of NiSi).

2. Device Fabrication

In this work, we fabricated NiSi SBDs with thicknesses of 1, 2, 3 and 4 nm in two different optical design configurations: frontside illumination (FSI) with backside reflector and backside illumination (BSI) with anti-reflection (AR) coating and quarter-wave resonant reflector. These device configurations are illustrated in Fig. 3. Wide-area companion samples were processed in parallel to provide

identical material stacks for optical characterization and comparison. These companion samples were always side-by-side to the corresponding device samples during every deposition process to ensure that the material stacks remained identical throughout all process sequences.

All devices were fabricated on [100] double-side polished (DSP) n-type silicon wafers with resistivity between 1–10 Ω·cm. A photoresist liftoff process is first used to define the detector area. After resist develop, a 4 min O_2 plasma was used to clear the surface of any organic residue. Immediately prior to the e-beam evaporation of Ni, a 20 s dilute BOE etch was used to eliminate any native oxide on the silicon surface. Ni film thickness was controlled using a quartz-crystal microbalance to be 0.5, 1, 1.5 and 2 nm, which combine with silicon to become 1, 2, 3 and 4 nm films of NiSi (respectively) after annealing at 400 C for 5 min [30], [31]. Attempts to fabricate NiSi SBDs from Ni films thinner than 0.5 nm resulted in devices with performance characteristics that suggested discontinuous NiSi films were formed, i.e., dark current that didn't scale with device area and absence of photo response. We've concluded from this result that the percolation threshold for NiSi is around 1 nm for our deposition and annealing conditions. Wide area Ti/Au ground contacts are then deposited using another liftoff process to form a relatively low impedance contact to the substrate as well as on the NiSi film for wire bonding. The FSI configuration is completed by depositing a 200 nm thick Al film on the backside of the substrate, after thorough cleaning, to form a high-quality mirrored surface. For the BSI devices, the process was continued by depositing a quarter-wave (258 nm at 1.55 μm wavelength) SiO_2 layer on top of the NiSi film using plasma-enhanced chemical vapor deposition (PECVD). A Cr/Au (5/200 nm) mirror is then deposited on top of the SiO_2 layer to complete the resonant reflector of the BSI configuration. To expose the contacts for wire bonding, the sample is etched in BOE with the Cr/Au metal stack functioning as an etch mask. The BSI configuration is completed with another quarter-wave PECVD SiO_2 layer on the backside of the wafer to function as an AR coating. For reference, a 100 nm thick NiSi SBD was also fabricated. This device was only tested in the BSI configuration because SBDs require hot carrier generation near the Schottky barrier interface to obtain reasonable collection efficiency.

3. Device Characterization and Analysis

3.1 Dark Current

Device dark current/voltage measurements were performed using an Agilent 4155C semiconductor parameter analyzer. Temperature-dependent dark current was measured by mounting the devices in a pour-filled liquid nitrogen cooled dewar with a LakeShore Cryogenics DT-470 silicon diode sensor for monitoring the device temperature.

Tight bunching of the reverse-bias dark current density for all of the devices/samples in Fig. 4(a) indicates excellent device uniformity, a favored characteristic of SBDs. The plot in Fig. 4(b) shows the dark current isn't affected by the device size, indicating edge effects are negligible in this size regime. The inset reveals no obvious correlation between the dark current and silicide thickness for the thin devices. This implies that any effect the silicide thickness has on dark current is minor relative to other parameters such as substrate doping and process nonuniformities/defects. Because these devices were fabricated on different wafers, with quoted resistivity between 1–10 Ω·cm, the substrate doping amongst the samples can also vary by an order of magnitude (between approximately 4.5e14 and 4.5e15 cm^{-3}). To quantify the impact of this variation on the dark current, we used the thermionic emission-driven dark current model [12]:

$$J = A^{**}T^2 \exp\left(-\frac{q\Phi_B(V)}{k_B T}\right)\left(1 - \exp\left(\frac{qV}{k_B T}\right)\right) \tag{1}$$

$$\Phi_B(V) = \Phi_{B0} - \sqrt{\frac{qE_m(V)}{4\pi\varepsilon_s}} - \alpha_s E_m(V) \tag{2}$$

where A^{**} is the effective Richardson constant (approximately 112 cm^{-2} for n-type SBDs), V is the bias voltage, Φ_{B0} is the intrinsic barrier height, E_m is the electric field and α_s is an empirical static
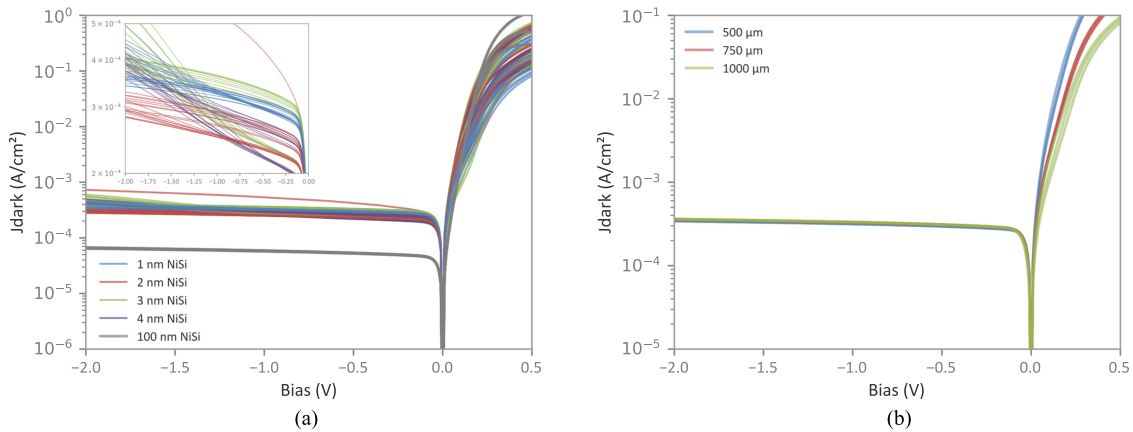
Fig. 4. (a) Dark current density plot of all (80) detectors at room temperature. The inset is a zoom view of the reverse bias region to better distinguish the distribution of curves for each NiSi thickness. (b) Room temperature dark current density of BSI 1 nm NiSi sample, color coded by device size, demonstrating negligible edge effects in this size regime. This size independence is consistent for all samples, but shown here using the devices from a single die for clarity.
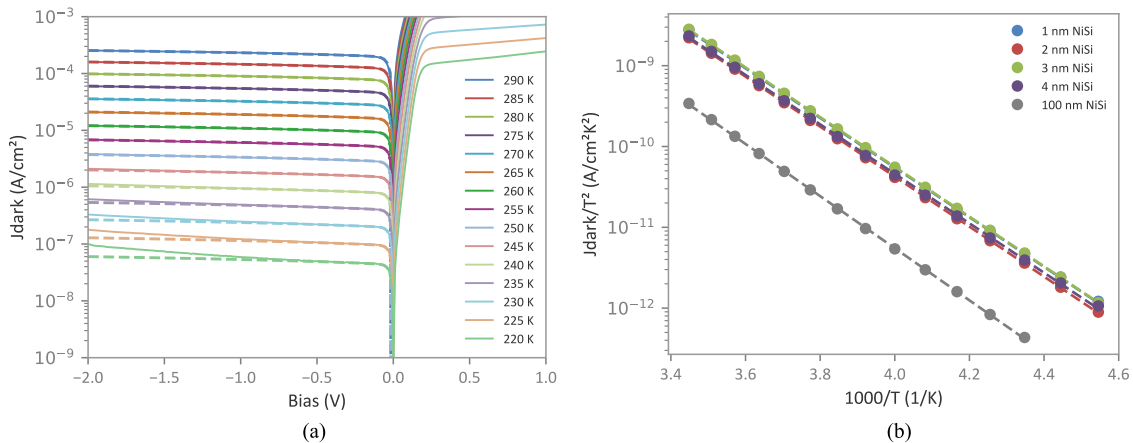

Fig. 5. (a) Modeled (dashed) and measured (solid) reverse-bias dark current density (BSI 1 nm NiSi device). (b) Arrhenius plot of BSI device dark current measured between 290 K and 220 K using 1 V reverse bias.

lowering coefficient. In the above formulation, we treat the barrier height as a voltage dependent quantity due to image force and static barrier lowering as described by Andrews and Lepselter [13]. Calculation of the voltage dependent electric field, based on the doping of the semiconductor and other material parameters, is detailed in [12]. A comparison of this model to temperature dependent measurements of one of the BSI 1 nm NiSi devices is included in Fig. 5(a). The agreement between the measured data and thermionic emission model with barrier height lowering effects is remarkably good; the deviation between experimental data and the model at lower temps and higher bias is attributed to tunneling mechanisms which aren't included in the model. The doping used to calculate the modeled dark current in the plotted device is 8.5e14 cm^{-3}. Adjusting the modeled doping to the two extremes afforded by the quoted resistivity of the wafers used for fabrication reveals a dark current of 1.5 times higher for the highest doped wafer relative to the lowest (1 V reverse bias). Because the dark current is also a strong function of temperature, we fixed the doping to 8.5e14 cm^{-3} and varied the temperature between 297 K and 294 K (reasonable estimate of room temperature fluctuation in our lab) and found the dark current to be a factor of 1.3 higher at 297 K (1 V reverse bias). Ignoring the single runaway device, the ratio between the highest and lowest

experimental dark current is 1.44 (at 1 V reverse bias) for the thin devices. Based on these results, we conclude that variations in substrate doping and chip temperature are sufficient to explain the variation in dark current observed by these devices. Process nonuniformities and defects are also likely to create minor variation between devices. To our knowledge, no SBD dark current model has been proposed that considers the device thickness as a parameter of interest, though it has been observed that ultra-thin SBDs can feature a lower SBH than thick devices [8], [11]. This shouldn't be interpreted as a fundamental increase in dark current however, because the smaller SBH also extends the photo-response to longer wavelengths and is described well by the standard dark current models, as indicted by Fig. 5(a). To characterize the effective SBH at the operation voltage used for quantum efficiency measurements in the subsequent sections, an Arrhenius analysis of every device was performed. The extracted activation energies for each device is included in Table 2 and plotted in Fig. 5(b) for the BSI devices. The activation energy of all thin devices was found to be within 5 meV of 610 meV. The 100 nm thick device featured a higher activation energy of 640 meV, explaining the lower dark current at room temperature relative to the thin devices.

3.2 External Quantum Efficiency

Spectral response measurements were made with a Thermo Scientific Nicolet 8700 FTIR spectrometer using the external detector input through a Keithley 428 current pre-amplifier. We used a deuterated L-alanine-doped triglycine sulfate (DLaTGS) pyroelectric detector to obtain a system reference spectrum. The raw pyro signal was corrected for its frequency response and divided by the photon energy to account for the optical power (rather than photon flux) linear dependence of the responsivity. The relative spectral response of the NiSi detectors is then obtained by simply dividing the raw response by the system reference spectrum. To measure quantum efficiency, a method detailed by J.D. Vincent [32] is used. A calibrated Infrared Systems Development Corp. IR-563/301 cavity blackbody at 1000 C provides a predictable source flux and spectrum according to Planck's Law. Narrowband optical filters are used to limit the flux to a narrow optical spectrum of interest. The source signal is modulated with an optical chopper wheel and the response monitored using a Keithley 428 current preamplifier and Stanford Research Systems SR850 DSP lock-in amplifier to isolate the signal from background noise. Spectral transmission of the window and optical filters were measured using the FTIR spectrometer, and accounted for in the QE calculation. Two QE measurements with different optical filters provide two scaling factors for the relative spectral response which are averaged to generate the QE spectrum. The QE spectrum of the FSI 2 nm NiSi device with superimposed spectral filters (scaled according to the QE measurement) is shown in the inset of Fig. 6; the agreement between the two optical measurements and spectral response curve shown in the inset was typical and consistent for all measurements.

As expected, QE for BSI devices is higher than FSI due to expected higher absorption (Fig. 6). The FSI devices feature an optimum NiSi thickness between 1–2 nm, while the BSI devices feature an optimum NiSi thickness between 1–3 nm. This result highlights the relationship between the detector optical design architecture and optimum silicide layer thickness for SBDs. Each combination of silicide and optical architecture, can have a unique optimal silicide thickness that maximizes QE whenever the absorption is incomplete (typical for thin silicide SBDs in an imaging configuration). Also evident in Fig. 6 is the substantial improvement of all sub 5 nm devices relative to the 100 nm reference device.

3.3 Internal Quantum Efficiency Measurement

QE is simply equal to the fractional absorption of light multiplied by the IQE, so accurately obtaining the absorption spectrum of these devices is all that remains to obtain the IQE spectra. The transfer-matrix method (TMM) can be used to precisely calculate the absorption of each layer of a film stack if the complex index of refraction over the wavelength range of interest is known for each layer [33], [34]. For this, a least-squares fitting (LSF) procedure was used to first determine index dispersion values for Si, SiO$_2$, Al, Cr, and Au (the collection of materials used in the FSI and BSI
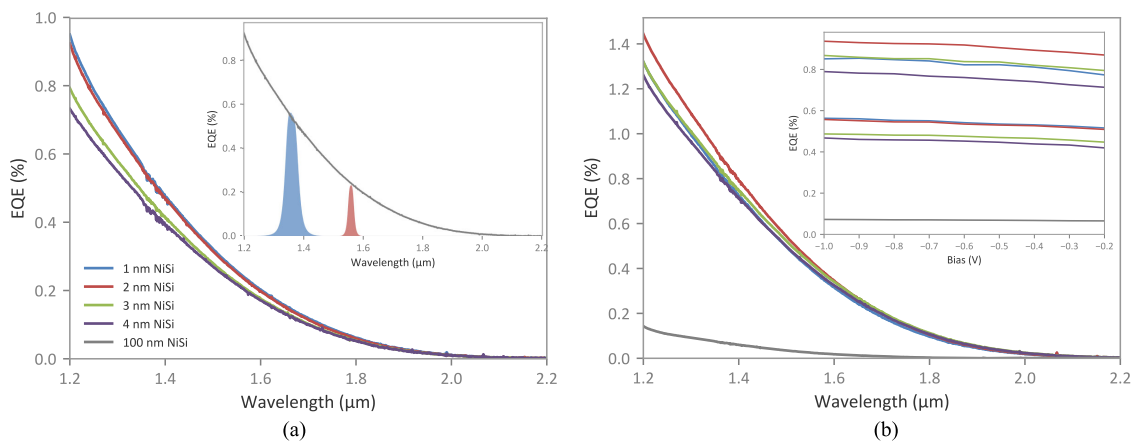
Fig. 6. QE spectra for the (a) FSI and (b) BSI devices at 1 V reverse bias. The inset in (a) demonstrates how two spectral notch filter measurements are used to scale the relative spectral response obtained by FTIR. The spectrum used for the inset is a 2 nm NiSi FSI device but is representative of the agreement obtained for all spectra. The inset in (b) shows the QE as a function of bias, illuminated through the blue (1.38 μm peak) notch filter; the BSI devices are the higher grouping of values, while the FSI devices are the lower grouping in this inset. All measurements were performed at room temperature.

configurations) using TMM to calculate the modeled transmission and reflection. The progression of fitting the various materials is illustrated in Fig. 7. The silicon band-edge was fit using the parabolic approximations described by [35], and free-carrier absorption was modeled as a simple power function [36]. The Cauchy model for transparent media was used to fit the real-part of the Si index as well as the SiO_2 index. Dispersion curves for the metals Al [37], Cr [38], and Au [39] were taken from literature and well-established databases [40]. The fitting process consists of taking an initial guess of the various parameters of the refractive index models, calculating the predicted reflection and transmission using TMM, calculating a residual error between the model and measured data (for each measurement at each wavelength), and forming a new guess for the models using a root finding algorithm loop until the residuals are sufficiently small. The root finding method we used for this fitting procedure is the trust region reflective method [41], which is generally robust and performed well for these datasets. The code used for the fitting was written in a way to enable fitting the index model parameters of a single film to multiple measurements that include that film simultaneously. We determined this multi-measurement approach was required to properly constrain the fitting and improve accuracy and consistency. While a single measurement can be used to fit the index parameters of a film, those parameters wouldn't reliably predict other measurements unless those measurements were included in the fitting simultaneously. This is analogous to taking measurements at multiple angles to improve fitting reliability with ellipsometry.

With all of the constituent materials modeled accurately to fit the FTIR measurements above, final fitting of the NiSi layers can be performed. Each thickness is fit independently of one another because it is known that material refractive index dispersion changes with thickness in the ultra-thin film regime [42], [43]. A polynomial of the following form was used to fit the NiSi index dispersion:

$$n + ik = C_1 + C_2\lambda + C_3\lambda^3 + i\left(C_4 + C_5\lambda + C_6\lambda^3\right) \tag{3}$$

For each layer thickness, reflection and transmission measurements of the NiSi thin film on Si as well as reflection measurements of the BSI and FSI configurations were used for fitting. All of this data along with the modeled fitting curves are plotted in Fig. 8. A summary of the converged fitting parameters for the NiSi films is provided in Table 1.

By implementing a fitting procedure to model the complex index of refraction for each material, we are able to accurately account for the parasitic losses due to free-carrier absorption in Si and losses in the metallic mirror layers to extract absorption in the NiSi layer. Because the NiSi film absorption
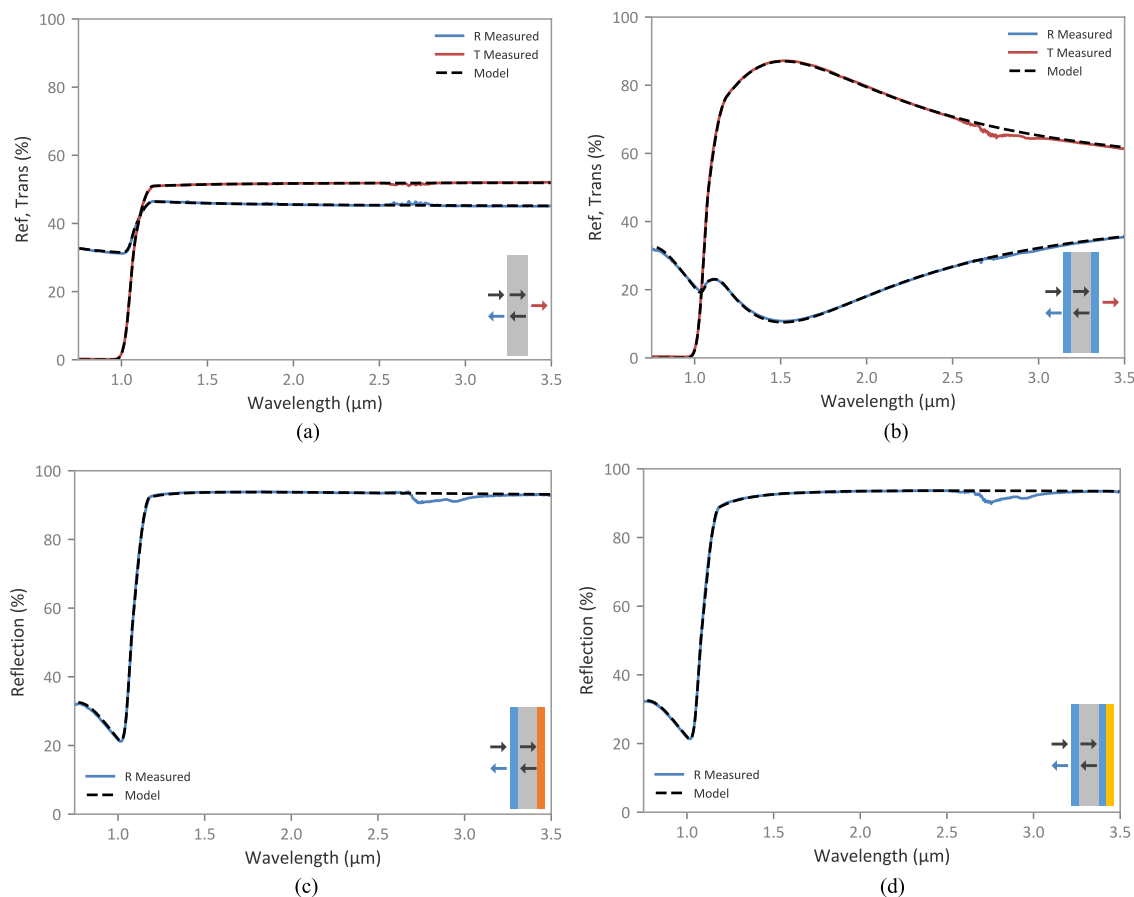
Fig. 7. Transmission and reflection spectra of companion pieces used to characterize the index dispersion of various thin films used in fabrication of the devices. (a) plots the measurements of a bare DSP silicon wafer, (b) plots an SiO_2 coated silicon wafer, (c) plots an SiO_2 coated silicon wafer with aluminum backside mirror representative of FSI devices, and (d) plots an SiO_2 coated silicon wafer with Cr/Au backside mirror representative of BSI devices.

TABLE 1

Refractive Index Parameters of NiSi films. These Parameters are Inserted Into the Polynomial Model From (3) to Calculate Absorption Using the TMM.

NiSi Film	C_1	C_2	C_3	C_4	C_5	C_6
1 nm	5.97	-1.48	0.0479	1.73e-9	3.56	-0.0211
2 nm	5.37	-0.756	0.106	-1.7e-6	3.79	-0.175
3 nm	4.87	-0.354	0.0754	2.46e-6	3.6	-0.141
4 nm	4.41	-0.165	0.0633	4.58e-7	3.44	-0.126
100 nm	5.76	-1.05	-1.3e-3	-2.22e-3	3.91	-0.0857

depends on the thickness, the parasitic losses are not constant amongst the samples/layers and must be modeled to account for those variations. The calculated absorption from each layer for both the FSI and BSI configurations is plotted for the 2nm NiSi film in Fig. 9.

Using this LSF/TMM method, we extract the complex index of refraction spectra for each layer. It should be noted that for incoherent layers (e.g., ultra-thin layers like the NiSi and thick layers like the Si substrate) the precision of determining the index spectra is dependent on the fidelity to which the layer thickness is known. This is because the thickness of these layers is too small

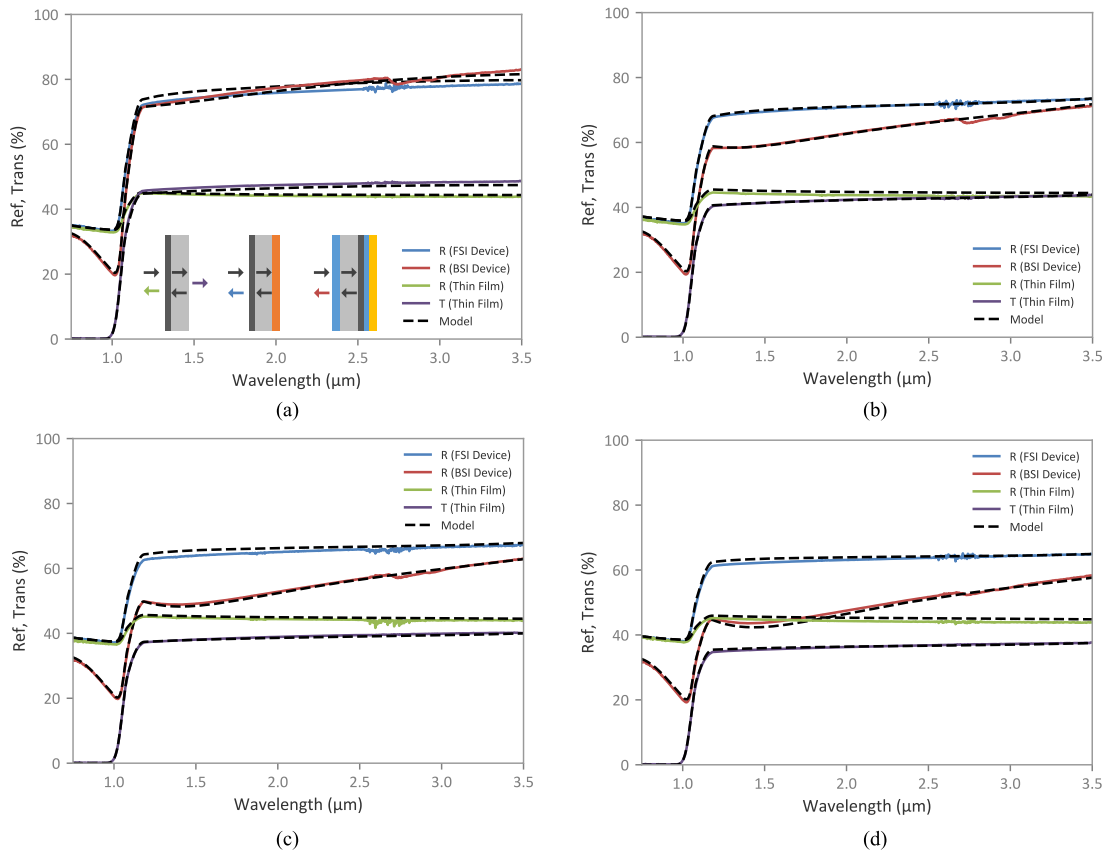Fig. 8. Reflection and transmission measurements and model fit for the (a) 1 nm, (b) 2 nm, (c) 3 nm, and (d) 4 nm NiSi films. Measurements of simply the NiSi thin film on silicon, the completed FSI device and the completed BSI device are all included for each thickness.
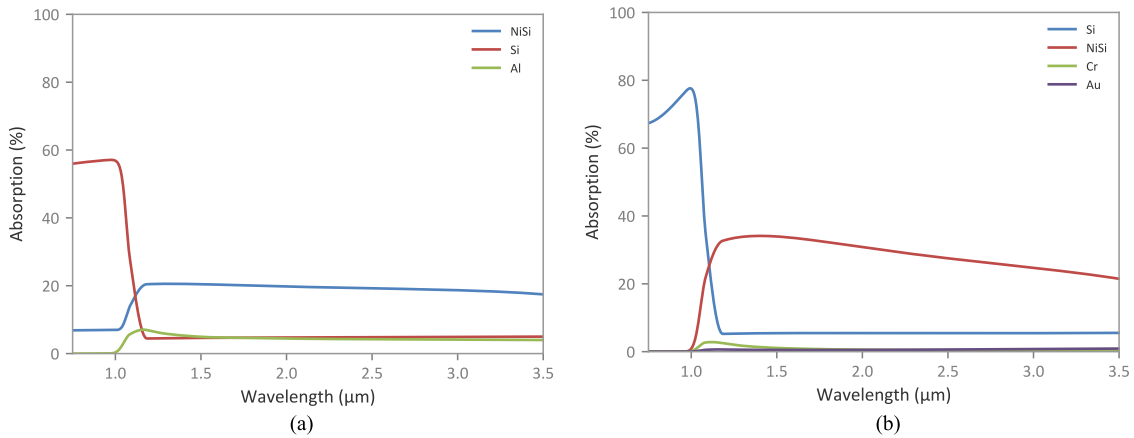

Fig. 9. Example calculation of the per-layer absorption for the 2 nm NiSi device in the (a) FSI and (b) BSI configurations.
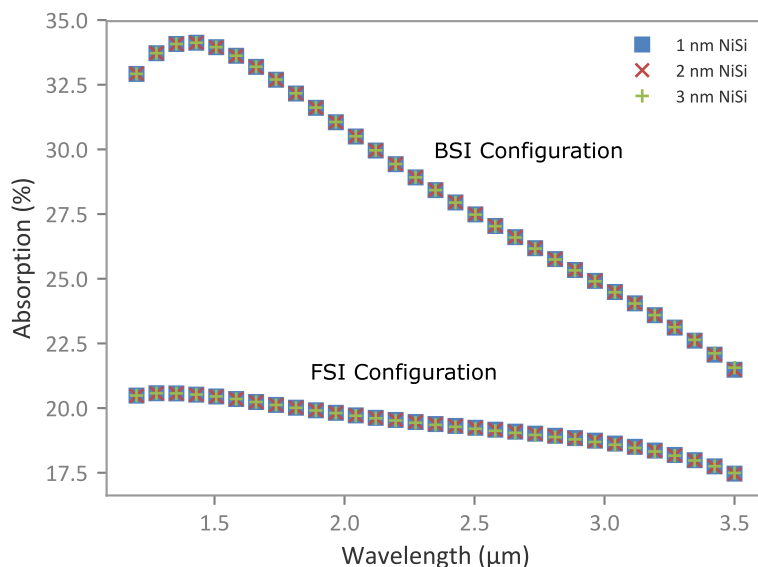
Fig. 10. The resultant absorption calculation of the 2 nm NiSi film in the BSI and FSI configurations, fitted as though the layer was 1, 2 and 3 nm thick.

(or too large) to contribute to interference fringing effects, and therefore thickness information isn't encoded in the measurement spectra and cannot be determined without an independent measurement of the thickness. This limitation is analogous to the challenge of fitting the film index and thickness simultaneously using ellipsometry of ultra-thin films [44]. For these samples, our independent measurement comes from a quartz-crystal thickness monitor during deposition. However, this limitation does not impact the method's ability to accurately determine the absolute absorption in each layer. This is perhaps obvious for the case of the thick substrate, where an adjustment to the substrate thickness will result in a change in the absorption coefficient such that total absorption is equivalent. We have found the equivalent to be true for the ultra-thin film case as well. To demonstrate this, the LSF/TMM procedure was repeated for the same set of FTIR measurements of the 2 nm NiSi film assuming the film thickness was 1, 2, and 3 nm (an overestimation of the error bounds on the film thickness). Fig. 10 demonstrates that while the absolute value of the index dispersion changes for each fitting, the calculated absolute absorption does not.

Because the goal of this fitting procedure is to extract an accurate representation of the absorption spectrum and not the refractive index dispersion, we find this method to be satisfactory despite its limitations. Again, considering the analogy of ellipsometry measurements of ultra-thin films, the ellipsometric quantities Δ, Ψ and ρ can be accurately determined readily from measurements while accuracy of the refractive index fitting is reliant on input of an accurate film thickness derived from another independent measurement. From this perspective, our method of LSF/TMM is potentially more useful for characterizing devices with ultra-thin films such as SBDs than ellipsometry because the measurable parameters of reflection, transmission and absorption are physically meaningful to device performance, while the ellipsometric quantities are not.

Using the calculated absorption spectra from the LSF/TMM technique along with the QE spectra, we can calculate the device IQE for both the FSI and BSI device configurations which is shown in Fig. 11.

Fig. 11 clearly depicts a trend of increasing IQE with decreasing NiSi thickness. We also see in the plot that the IQE for both the FSI and BSI configurations are in good agreement for all four NiSi thicknesses tested. This result suggests that absorption in the film is relatively uniform as a function of depth, i.e., no significant gradients in the density of excited carriers exist within the
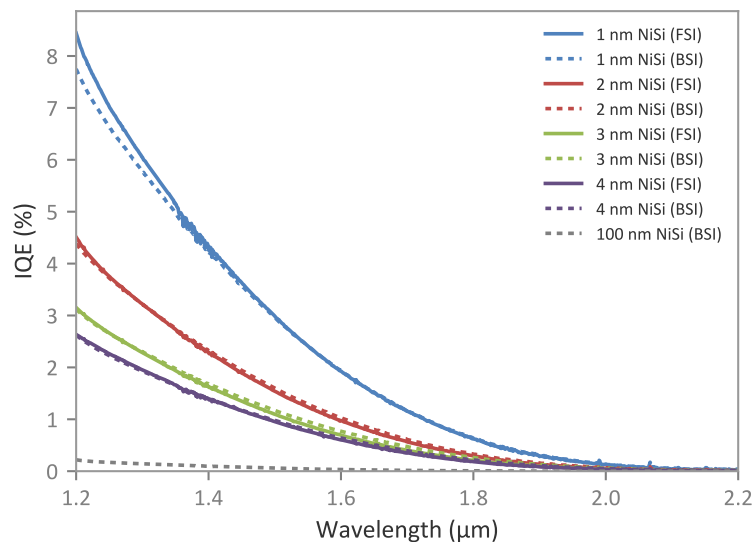
Fig. 11. Calculated IQE spectra for all FSI and BSI devices (1 V reverse bias). IQE is calculated from the QE spectral measurement and absorption calculation based on the film FTIR measurements.

film under illumination. Good agreement of the IQE between the BSI and FSI configuration also provides confidence in the accuracy of these results and demonstrates the utility of the method for determining IQE. IQE of the 1 nm NiSi device was found to be 2.4% and 5.9% at 1.55 μm and 1.3 μm respectively, an improvement factor of 16.7 over the highest previously reported value of 0.144% at 1.55 μm [20] with a comparable SBH in NiSi, and a factor of 57 improvement over the 100 nm thick reference device we fabricated.

3.4 Internal Quantum Efficiency Analysis

A common method for characterizing the quantum yield of SBDs is in relation to the modified Fowler equation [45]:

$$IQE = C\frac{(h\upsilon-\Phi_B)^2}{h\upsilon} \qquad (4)$$

where C is the quantum efficiency coefficient (eV^{-1}) and $h\upsilon$ is the photon energy. The Fowler equation therefore enables a simple linear fitting of the SBH and quantum efficiency coefficient, which is independent of the photon energy, directly from a response measurement. While it is common to use the QE when fitting to the Fowler plot, ideally the detector IQE spectrum should be used because the modified Fowler equation does not consider absorption.

The plot in Fig. 12(a) shows the devices fit the Fowler yield relationship well over a wide range of photon energies, but deviates when the photon energy approaches the SBH. Because the Fowler quantum efficiency coefficient (C) is wavelength-independent measure of the quantum yield, it is a useful parameter to compare as a function of the silicide thickness as shown in Fig. 12(b). From this plot we can see good agreement between the FSI and BSI quantum yield across the thickness range. The shape of the plot suggests that the quantum yield parameter is accelerating rather than saturating with decreasing thickness across the range tested. The implication of this result is that further improvement to the quantum yield should be realizable if the NiSi thickness can be reduced from what has been demonstrated here.

The modified Fowler equation approximates the Vickers' model [46] as device temperature approaches zero. This is a fairly good approximation for cryogenically cooled SBDs and for photon energies much larger than the barrier height, but isn't a strictly accurate approximation for moderate barrier heights at room temperature. Nevertheless, the fitting is included above because of its widespread use in the field and its simplicity for analysis and comparison. A more meaningful
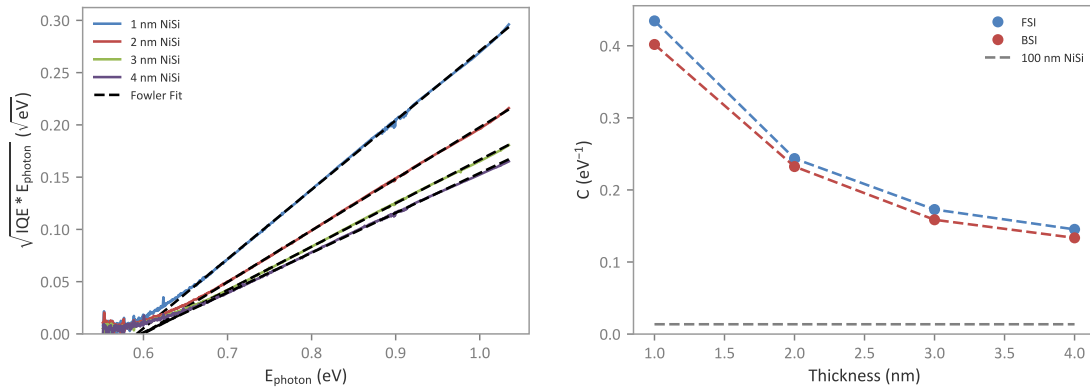
Fig. 12. (a) Fowler plot of 1, 2, 3 and 4 nm NiSi FSI photodetectors. (b) Quantum efficiency coefficient dependence on thickness for FSI and BSI devices, the 100 nm thick NiSi quantum efficiency coefficient value is included for reference as the grey dotted line and should not be interpreted as a function of thickness.

investigation of the SBD quantum efficiency would consider the effect of carrier scattering and the film thickness to explain the thickness dependence of the quantum efficiency. Vickers' model, in its general form, does exactly this:

$$IQE = P(t) \cdot F(\Phi_B) \tag{5}$$

where $F(\Phi_b)$ is the Fowler Factor and $P(t)$ is the thickness-dependent scattering term. The Fowler factor describes the fraction of hot carriers whose energy and momentum satisfy emission over the barrier. Vickers' derived formula for the Fowler factor includes a computationally expensive polylogarithm function which makes it impractical for experimental fitting. The approximation of this factor as temperature approaches zero, reduces to the Fowler equation which is typically modified further to include the quantum efficiency coefficient for empirical fitting to experimental data. The scattering term describes the probability that carriers with sufficient energy are scattered off of phonons or the metal interfaces until the momentum also satisfies emission before it collides with another carrier and loses its energy. It is from this term that the theory of increased collection efficiency with decreasing film thickness is quantified. The rigorous model proposed by Vickers is again complex, which includes exponential integral functions that again make experimental fitting difficult. Vickers also proposes an approximation to the model that simplifies computation, but the approximation loses accuracy for ultra-thin metal layers. Recently, Casalino has addressed the challenges with Vickers' rigorous model by developing approximate formulas for the Fowler Factor and scattering term that significantly improve the accuracy relative to the approximations described above while preserving the thickness-dependent scattering term [47].

$$P(t) = \frac{L}{t}\left(\sqrt{1 - e^{-\frac{t}{L}}} + 0.1 \cdot e^{-4.1\frac{t}{L}}\right) \tag{6}$$

$$F(\Phi_B) = \frac{1}{4E_F h\upsilon}\left(\frac{(h\upsilon - \Phi_B)^2}{2} + (k_B T)^2 \cdot \left(\frac{\pi^2}{6} - 1.545 \cdot e^{-1.07\frac{h\upsilon - \Phi_B}{k_B T}} + 0.722 \cdot e^{-1.07\frac{h\upsilon - \Phi_B}{k_B T}}\right)\right) \tag{7}$$

Using Eqn. (6) and (7) as inputs to (5) provides a long but computationally efficient expression for the device IQE that can be used as a physical model for fitting. Despite all the terms, the only unknown variables in this expression are the NiSi Fermi energy E_F (4.35 eV [48]), the SBH Φ_B and the hot carrier mean free path L. Rather than defining the NiSi thickness and fitting the mean free path, we've chosen to fit to the ratio of the mean free path and thickness.

Using a least-squares fitting procedure, we were able to extract the SBH and L/t ratio for each device using Casalino's approximation to Vickers' model as shown in Fig. 13. The advantage of this approach over the more common Fowler fitting is the improved agreement between theory and
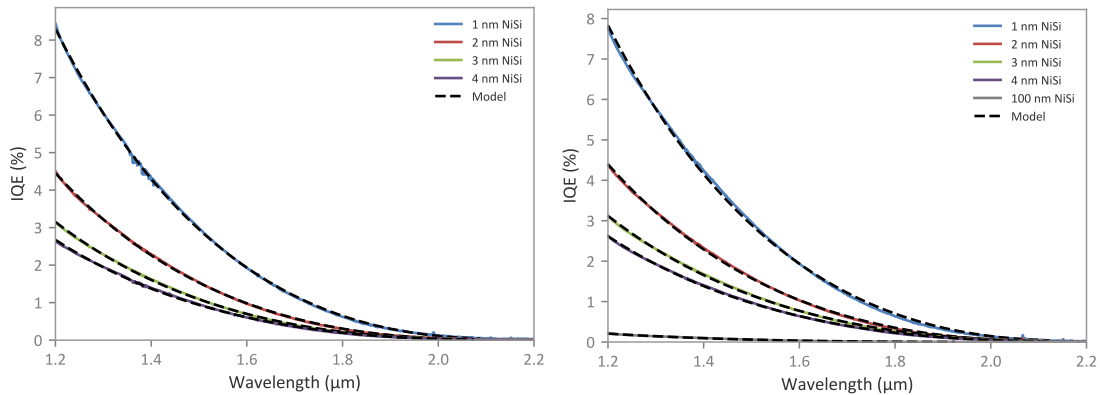
Fig. 13. Fowler plot IQE fitting of (a) FSI and (b) BSI NiSi devices using Casalino's approximation of Vickers' model.

TABLE 2

Summary of Measured and Extracted Parameters From NiSi SBDs. Φ_{BF}, Φ_{BV} and Φ_{BA} are the Extracted SBH Using the Modified Fowler Equation, Casalino's Vickers Approximation and Arrhenius Analysis (IVT) Respectively. All Voltage Dependent Quantities, Such as the Quantum Efficiency, are for a 1 V Reverse Bias.

Device	Modified Fowler		Vickers' Model			Arrhenius	Calculated from Measurement			
	C (eV^{-1})	Φ_{BF} (eV)	L/t	L (nm)	Φ_{BV} (eV)	Φ_{BA} (eV)	$QE_{1.3\mu m}$ (%)	$IQE_{1.3\mu m}$ (%)	$QE_{1.55\mu m}$ (%)	$IQE_{1.55\mu m}$ (%)
1 nm (FSI)	0.435	0.59	72.5	72.5	0.595	0.607	0.67	6.05	0.26	2.41
1 nm (BSI)	0.402	0.583	63.2	63.2	0.585	0.610	1.0	5.78	0.4	2.41
2 nm (FSI)	0.244	0.599	32.7	65.4	0.603	0.610	0.66	3.22	0.25	1.23
2 nm (BSI)	0.232	0.59	30.1	60.2	0.593	0.613	1.09	3.22	0.44	1.29
3 nm (FSI)	0.173	0.599	19.9	59.7	0.602	0.610	0.58	2.28	0.22	0.88
3 nm (BSI)	0.159	0.582	17.5	52.5	0.584	0.612	1.01	2.3	0.43	0.96
4 nm (FSI)	0.145	0.596	15.3	61.2	0.598	0.605	0.55	1.95	0.22	0.77
4 nm (BSI)	0.133	0.583	13.7	54.8	0.586	0.608	0.96	1.92	0.41	0.8
100 nm (BSI)	0.014	0.639	0.53	58.0	0.645	0.640	0.09	0.14	0.03	0.04

experimental (when the photon energy is near the barrier height) and the extraction of the physically meaningful L/t ratio. A summary of all of all of the extracted device parameters is included in Table 2.

As expected, the L/t ratio monotonically increases with decreasing NiSi thickness. The average hot carrier mean-free path for the BSI and FSI devices was found to be 57.7 nm and 64.7 nm respectively. This result is consistent with the modified Fowler fit where the average quantum efficiency coefficient is slightly higher for the FSI devices than the BSI. While this could suggest the BSI device NiSi films have been degraded slightly, we are hesitant to draw that conclusion. Both the modified Fowler fitting as well as the fitting to Casalino's Vickers approximation lose accuracy as the photon energy approaches the barrier height. We found both methods underestimated the measured zero-crossing wavelength of the QE spectrum (over-estimation of Φ_B) which was found to be around 2.15 μm ($\Phi_B = 0.577$ eV) for all devices. In contrast, both models fit the SBH of BSI devices to be smaller than the FSI devices. Additionally, inspection of the IQE in Fig. 11 and Table 2 suggests that the collection efficiency between FSI and BSI are quite similar. Discrepancies between the IQE of FSI and BSI devices for a given thickness are not consistently in favor of one illumination configuration over the other when considering the full wavelength range. For this

reason, we interpret the extracted L to be an approximation limited in accuracy by the approximate model used for fitting as well as the accuracy of the film thickness, which is difficult to measure with high precision in this thickness regime. Despite this limitation, we believe fitting SBD device performance to a physical model that includes L to be a more meaningful and insightful than simply using a fitting parameter, as is more typically done with these devices, using the modified Fowler fit.

4. Summary and Conclusion

We have fabricated and characterized a series of NiSi/n-Si SBDs in two imaging configurations (FSI and BSI) with silicide thicknesses of 1, 2, 3, 4 and 100 nm. We found the IQE to monotonically increase with decreasing silicide thickness. Efforts to fabricate SBDs with silicide thickness below 1 nm resulted in IV and QE characteristics that suggest a discontinuous NiSi film was formed. We believe additional improvement to the IQE is possible if thinner NiSi layers can be reliably fabricated by adjusting the deposition/annealing process appropriately. This is evidenced by an accelerating increase in the quantum efficiency coefficient with decreasing silicide thickness obtained by fitting device IQE to the modified Fowler equation. Further insight into the hot carrier transport properties was obtained by fitting the IQE to an approximation of Vickers' model provided by Casalino. To our knowledge, this is the first extraction of the hot carrier mean-free path directly from SBD device measurements ($\sim$60 nm for electrons in NiSi). The IQE measurements were enabled by a simultaneous multi-measurement reflection/transmission fitting that we used to extract the silicide absorption by accounting for parasitic losses in the substrate and metallic mirrors. Using this method, we found parasitic losses were not negligible and hope future SBD characterization reports adopt similar methodology rather than simply assuming all loss is due to the silicide layer, which we found to be inaccurate. We expect that SBDs fabricated near the percolation threshold, with novel approaches to maximizing absorption such as photonic and plasmonic resonators or waveguided structures, have the greatest promise of maximizing the potential of this low-cost IR detector technology.

Acknowledgment

References

[1] H. Elabd, T. Villani, and W. Kosonocky, "Palladium-silicide Schottky-barrier IR-CCD for SWIR applications at intermediate temperatures," *IEEE Electron Device Lett.*, vol. 3, no. 4, pp. 89–90, Apr. 1982.
[2] F. D. Shepherd and A. C. Yang, "Silicon Schottky retinas for infrared imaging," in *Proc. Int. Electron Devices Meeting*, 1973, pp. 310–313.
[3] W. F. Kosonocky, F. V. Shallcross, T. S. Villani, and J. V. Groppe, "160 × 244 element PtSi Schottky-barrier IR-CCD image sensor," *IEEE Trans. Electron Devices*, vol. 32, no. 8, pp. 1564–1573, Aug. 1985.
[4] M. Kimata, M. Denda, N. Yutani, S. Iwade, and N. Tsubouchi, "A 512 × 512-element PtSi Schottky-barrier infrared image sensor," *IEEE J. Solid-State Circuits*, vol. 22, no. 6, pp. 1124–1129, Dec. 1987.
[5] A. Akiyama *et al.*, "1040 × 1040 infrared charge sweep device imager with PtSi Schottky-barrier detectors," *Opt. Eng.*, vol. 33, no. 1, pp. 64–71, Jan. 1994.
[6] M. Kimata *et al.*, "Platinum silicide Schottky-barrier IR-CCD image sensors," *Jpn. J. Appl. Phys.*, vol. 21, no. 1, pp. 231–235, 1982.
[7] M. Kimata, T. Ozeki, N. Tsubouchi, and S. Ito, "PtSi Schottky-barrier infrared focal plane arrays," *Proc. SPIE*, vol. 3505, pp. 2–12, 1998.
[8] D. Worle *et al.*, "Amorphous and crystalline IrSi Schottky barriers on silicon," *Appl. Phys. A*, vol. 66, no. 6, pp. 629–637, Jun. 1998.
[9] B. Y. Tsaur, M. M. Weeks, R. Trubiano, P. W. Pellegrini, and T. R. Yew, "IrSi Schottky-barrier infrared detectors with 10-mu m cutoff wavelength," *IEEE Electron Device Lett.*, vol. 9, no. 12, pp. 650–653, Dec. 1988.
[10] B. Y. Tsaur, C. K. Chen, and B. A. Nechay, "IrSi Schottky-barrier infrared detectors with wavelength response beyond 12-mu m," *IEEE Electron Device Lett.*, vol. 11, no. 9, pp. 415–417, Sep. 1990.
[11] K. M. Mahlein, D. Woerle, T. Hierl, and M. Schulz, "Ultrathin Ir_3Si_4 silicide films for infrared detection," *Proc. SPIE*, vol. 3436, pp. 138–147, 1998.
[12] S. M. Sze and K. K. Ng, *Physics of Semiconductor Devices*, 3rd ed. Hoboken, NJ, USA: Wiley, 2007, p. 791.

[13] J. M. Andrews and M. P. Lepselter, "Reverse current-voltage characteristics of metal-silicide Schottky diodes," *Solid-State Electron.*, vol. 13, no. 7, pp. 1011–1023, 1970.

[14] M. Casalino, G. Coppola, M. Iodice, I. Rendina, and L. Sirleto, "Critically coupled silicon Fabry–Perot photodetectors based on the internal photoemission effect at 1550 nm," *Opt. Exp.*, vol. 20, no. 11, pp. 12599–12609, May 2012.

[15] M. Casalino *et al.*, "Cu/p-Si Schottky barrier-based near infrared photodetector integrated with a silicon-on-insulator waveguide," *Appl. Phys. Lett.*, vol. 96, no. 24, Jun. 2010, Art. no. 241112.

[16] M. W. Knight *et al.*, "Embedding plasmonic nanostructure diodes enhances hot electron emission," *Nano Lett.*, vol. 13, no. 4, pp. 1687–1692, Apr. 2013.

[17] I. Goykhman, B. Desiatov, J. Khurgin, J. Shappir, and U. Levy, "Locally oxidized silicon surface-plasmon Schottky detector for telecom regime," *Nano Lett.*, vol. 11, no. 6, pp. 2219–2224, Jun. 2011.

[18] S. Roy, K. Midya, S. P. Duttagupta, and D. Ramakrishnan, "Nano-scale NiSi and n-type silicon based Schottky barrier diode as a near infra-red detector for room temperature operation," *J. Appl. Phys.*, vol. 116, no. 12, Sep. 2014, Art. no. 124507.

[19] A. Sobhani *et al.*, "Narrowband photodetection in the near-infrared with a plasmon-induced hot electron device," *Nature Commun.*, vol. 4, Mar. 2013, Art. no. 1643.

[20] S. Y. Zhu, M. B. Yu, G. Q. Lo, and D. L. Kwong, "Near-infrared waveguide-based nickel silicide Schottky-barrier photodetector for optical communications," *Appl. Phys. Lett.*, vol. 92, no. 8, Feb. 2008, Art. no. 081103.

[21] M. W. Knight, H. Sobhani, P. Nordlander, and N. J. Halas, "Photodetection with active optical antennas," *Science*, vol. 332, no. 6030, pp. 702–704, May 2011.

[22] S. X. Li, N. G. Tarr, and P. Berini, "Schottky photodetector integration on LOCOS-defined SOI waveguides," *Proc. SPIE*, vol. 7750, 2010, Art. no. 77501M.

[23] M. Casalino, L. Sirleto, L. Moretti, M. Gioffre, G. Coppola, and I. Rendina, "Silicon resonant cavity enhanced photodetector based on the internal photoemission effect at 1.55 mu m: Fabrication and characterization," *Appl. Phys. Lett.*, vol. 92, no. 25, Jun. 2008, Art. no. 251104.

[24] P. Berini, A. Olivieri, and C. K. Chen, "Thin Au surface plasmon waveguide Schottky detectors on p-Si," *Nanotechnology*, vol. 23, no. 44, Nov. 2012, Art. no. 444011.

[25] C. K. Chen, B. Nechay, and B. Y. Tsaur, "Ultraviolet, visible, and infrared response of PtSi Schottky-barrier detectors operated in the front-illuminated mode," *IEEE Trans. Electron Devices*, vol. 38, no. 5, pp. 1094–1103, May 1991.

[26] W. J. Chen, T. Kan, Y. Ajiki, K. Matsumoto, and I. Shimoyama, "NIR spectrometer using a Schottky photodetector enhanced by grating-based SPR," *Opt. Exp.*, vol. 24, no. 22, pp. 25797–25804, Oct. 2016.

[27] M. A. Nazirzadeh, F. B. Atar, B. B. Turgut, and A. K. Okyay, "Random sized plasmonic nanoantennas on silicon for low-cost broad-band near-infrared photodetection," *Sci. Rep.*, vol. 4, Nov. 2014, Art. no. 7103.

[28] A. Akbari, R. N. Tait, and P. Berini, "Surface plasmon waveguide Schottky detector," *Opt. Exp.*, vol. 18, no. 8, pp. 8505–8514, Apr. 2010.

[29] C. Scales and P. Berini, "Thin-film Schottky barrier photodetector models," *IEEE J. Quantum Electron.*, vol. 46, no. 5, pp. 633–643, May 2010.

[30] J. P. Gonchond *et al.*, "Combined XRR and R-S measurements of nickel silicide films," in *Proc. 5th Conf. Characterization Metrology ULSI Technol.*, Richardson, TX, USA, 2005, vol. 788, pp. 182–186.

[31] K. de Keyser *et al.*, "Phase formation and thermal stability of ultrathin nickel-silicides on Si(100)," *Appl. Phys. Lett.*, vol. 96, no. 17, Apr. 2010, Art. no. 173503.

[32] J. D. Vincent, *Fundamentals of Infrared Detector Operation and Testing*, New York, NY, USA: Wiley, 1990.

[33] S. J. Byrnes, "Multilayer optical calculations," 2016, arXiv:1603.02720v2.

[34] S. J. Byrnes, *tmm.py 0.1.7*, 2017. [Online]. Available: https://pypi.org/project/tmm/

[35] F. Stern, "Dispersion of index of refraction near absorption edge of semiconductors," *Phys. Rev.*, vol. 133, no. 6A, pp. A1653–A1664, 1964.

[36] R. R. Vardanyan, V. K. Dallakyan, U. Kerst, and C. Boit, "Modeling free carrier absorption in silicon," *J. Contemporary Phys. Armenian Acad. Sci.*, vol. 47, no. 2, pp. 73–79, Apr. 2012.

[37] M. A. Ordal, R. J. Bell, R. W. Alexander, L. A. Newquist, and M. R. Querry, "Optical-properties of Al, Fe, Ti, Ta, W, and Mo at submillimeter wavelengths," *Appl. Opt.*, vol. 27, no. 6, pp. 1203–1208, Mar. 1988.

[38] A. D. Rakic, A. B. Djurisic, J. M. Elazar, and M. L. Majewski, "Optical properties of metallic films for vertical-cavity optoelectronic devices," *Appl. Opt.*, vol. 37, no. 22, pp. 5271–5283, Aug. 1998.

[39] R. L. Olmon *et al.*, "Optical dielectric function of gold," *Phys. Rev. B*, vol. 86, no. 23, Dec. 2012, Art. no. 235147.

[40] M. N. Polyanskiy, *Refractive Index Database*. [Online]. Available: https://refractiveindex.info

[41] M. A. Branch, T. F. Coleman, and Y. Y. Li, "A subspace, interior, and conjugate gradient method for large-scale bound-constrained minimization problems," *SIAM J. Sci. Comput.*, vol. 21, no. 1, pp. 1–23, Sep. 1999.

[42] H. Brahmi *et al.*, "Electrical and optical properties of sub-10 nm nickel silicide films for silicon solar cells," *J. Phys. D, Appl. Phys.*, vol. 50, no. 3, Jan. 2017, Art. no. 035102.

[43] F. Nava *et al.*, "Electrical and optical-properties of silicide single-crystals and thin-films," *Mater. Sci. Rep.*, vol. 9, no. 4/5, pp. 141–200, Feb. 1993.

[44] M. M. Ibrahim and N. M. Bashara, "Parameter-correlation and computational considerations in multiple-angle ellipsometry," *J. Opt. Soc. Amer.*, vol. 61, no. 12, pp. 1622–1629, 1971.

[45] R. H. Fowler, "The analysis of photoelectric sensitivity curves for clean metals at various temperatures," *Phys. Rev.*, vol. 38, no. 1, pp. 45–56, Jul. 1931.

[46] V. E. Vickers, "Model of Schottky barrier hot-electron-mode photodetection," *Appl. Opt.*, vol. 10, no. 9, pp. 2190–2192, 1971.

[47] M. Casalino, "Internal photoemission theory: Comments and theoretical limitations on the performance of near-infrared silicon Schottky photodetectors," *IEEE J. Quantum Electron.*, vol. 52, no. 4, Apr. 2016, Art. no. 4000110.

[48] N. Biswas, J. Gurganus, and V. Misra, "Work function tuning of nickel silicide by co-sputtering nickel and silicon," *Appl. Phys. Lett.*, vol. 87, no. 17, Oct. 2005, Art. no. 171908.